β-decay feeding intensity distributions for ^{103,104m}Nb

J. Gombas [1,2,*] P. A. DeYoung [1,†] A. Spyrou, [2,3,4,‡] A. C. Dombos, [2,3,4] A. Algora [5,6] T. Baumann [3] B. Crider [3]
J. Engel [7] T. Ginter, [3] E. Kwan, [3] S. N. Liddick, [3,4,8] S. Lyons [3,4,§] F. Naqvi, [3,4] E. M. Ney [7] J. Pereira, [3,4] C. Prokop, [3,8]
W. Ong, [3,2,4] S. Quinn, [2,3,4] D. P. Scriven [2] A. Simon, [9] and C. Sumithrarachchi [3]

[1]*Department of Physics, Hope College, Holland, Michigan 49422, USA*
[2]*Department of Physics and Astronomy, Michigan State University, East Lansing, Michigan 48824, USA*
[3]*National Superconducting Cyclotron Laboratory, Michigan State University, East Lansing, Michigan 48824, USA*
[4]*Joint Institute for Nuclear Astrophysics, Michigan State University, East Lansing, Michigan 48824, USA*
[5]*Instituto de Física Corpuscular, CSIC–Universidad de Valencia, E-46071 Valencia, Spain*
[6]*Institute of Nuclear Research of the Hungarian Academy of Sciences, Debrecen H-4026, Hungary*
[7]*Department of Physics, University of North Carolina, Chapel Hill, North Carolina 27514, USA*
[8]*Department of Chemistry, Michigan State University, East Lansing, Michigan 48824, USA*
[9]*Department of Physics and Joint Institute for Nuclear Astrophysics, University of Notre Dame, Notre Dame, Indiana 46556, USA*

The β decays of ^{103,104m}Nb were studied with the Summing NaI(Tl) (SuN) detector at the National Superconducting Cyclotron Laboratory. The β-decay feeding intensity distribution $I_\beta(E)$ for each isotope was extracted by measuring γ rays in coincidence with an emitted electron. The $I_\beta(E)$ was extracted via the total absorption spectroscopy technique. The $I_\beta(E)$ for each nucleus was compared to predictions made by the quasiparticle random-phase approximation (QRPA) model which is commonly used to calculate β-decay properties for astrophysical applications. The main goal was to provide experimental data for neutron-rich nuclei, relevant to the astrophysical r process. In addition, the extracted β-decay feeding intensity distributions can lead to a better understanding of nuclear structure in a region of rapid structure changes around $A = 100$. Finally, experimental data for ^{104m}Nb are also of interest to antineutrino studies of nuclear reactors.

I. INTRODUCTION

Significant effort has been dedicated to the understanding of the origin of the elemental abundance distribution that is observed today in the universe. The rapid neutron-capture process (r process) and the slow neutron-capture process (s process) are responsible for the formation of most of the nuclei heavier than iron, each accounting for about half of the observed elemental abundance distribution. They were both introduced in the 1950s [1,2] together with a third process, the so-called p process, that is needed to explain the production of a small number of proton-rich isotopes [3,4]. While the s process has well known astrophysical sites, the astrophysical locations of the r and p processes are not well known. The present work focuses on the nuclear physics input necessary to describe the r process and identify its possible site(s).

Two main sites have been debated for decades, namely core-collapse supernovae and neutron-star mergers. The first observation of a neutron-star merger event in 2017 [5] and the kilonova signature that accompanied it [6] showed strong evidence that neutron-star mergers are at least one of the sites for the r process. This conclusion was also confirmed by the recent identification of Sr lines from the same event [7].

Astrophysical r-process calculations aim to reproduce the observed isotopic abundance distribution [8]. These calculations are sensitive to β-decay half lives, masses, β-delayed neutron emission probabilities, neutron capture cross sections, and fission properties [9]. These nuclear properties have not been determined experimentally for most nuclei involved in the r process, and astrophysical calculations rely heavily on nuclear models. The present work focuses on β-decay properties for which the quasiparticle random-phase approximation (QRPA) is the most commonly used model in astrophysical calculations [10].

It is essential to compare theoretical calculations to experimental data, where those are available, to test the reliability of the models and estimate their limitations when applied to nuclei that are still out of experimental reach. In particular for β-decay properties, QRPA calculations are typically compared to measured β-decay half lives and β-delayed neutron emission probabilities. These are integral quantities, and therefore a more sensitive constraint for QRPA calculations would be the β-decay and electron-capture strengths [10–12].

In addition to astrophysical and nuclear structure applications, the total absorption γ-ray spectra provided in this

––––––––––
[*]gombasja@msu.edu
[†]deyoung@hope.edu
[‡]spyrou@frib.msu.edu
[§]Present address: Pacific Northwest National Laboratory, Richland, WA 99354, USA.

study are of use in antineutrino studies in nuclear reactors. The International Atomic Energy Agency has deemed a total absorption spectroscopy (TAS) study of ^{104m}Nb as a "priority II" with regards to determining antineutrino energy spectra from nuclear reactors (see Tables 2 and 3 of Ref. [13]).

Here we present the first extraction of the β-decay strength for the isotopes ^{103,104m}Nb, by measuring the β-decay feeding intensity distribution, $I_\beta(E)$. The experimental results are compared to QRPA predictions for $I_\beta(E)$ and the Gamow-Teller transition strength, B(GT), distributions for the two isotopes of interest.

II. EXPERIMENTAL DETAILS

The experiment was conducted at the National Superconducting Cyclotron Laboratory at Michigan State University. A ^{124}Sn^{45+} beam collided with a 403 mg/cm^2 thick beryllium production target to produce secondary beams. These secondary beams were sent through the A1900 fragment separator [14] with a momentum acceptance of 5%. The atomic numbers of the filtered beam ranged between 39 and 43. The mass numbers ranged between 100 and 110. A thin, position-sensitive, plastic scintillator (I2SCI) served as the start in the time-of-flight (ToF) measurements which were used to identify the isotopes in the beam on an event-by-event basis.

After the A1900 fragment separator, the secondary beam was directed downstream to the experimental vault. The beam sequentially deposited energy into two silicon PIN detectors, the first of which was used as the stop in the ToF measurements. The silicon PIN detectors were 488 and 503 μm thick. Effective thicknesses of 637 and 657 μm were achieved by rotating both detectors 40°.

Due to the large momentum acceptance, it was necessary to correct the ToF measurements. Some particles took slightly longer paths. By using the measured position in the I2SCI, which is correlated with the path length of the particle, particles that took longer paths had their ToF decreased and those with shorter paths had their ToF increased. This new corrected ToF is then proportional to particle mass.

The particle identification was then done based on energy-loss measurements in the first PIN detector and the corrected ToF measurements between the I2SCI and the first PIN detector. The particle identification plot for this analysis can be seen in Fig. 1. Since the momentum acceptance of the A1900 fragment separator was set to 5%, several nuclei were found in the secondary beam [15,16]. This paper focuses on ^{103,104m}Nb. The half-lives of the isotopes in the cocktail beam were studied in an earlier publication by Dombos *et al.* [16].

The cocktail beam was implanted in a position-sensitive double-sided silicon-strip detector (DSSD). The DSSD was 20 mm by 20 mm with a thickness of 1030 μm. The DSSD had 16 strips on the front side and 16 orthogonal strips on the back. The position of each implanted nucleus could therefore be measured in the DSSD with a resolution of 1.25 mm. The DSSD measured both the energy deposited by implanting particles and the energy of emitted electrons from subsequent β decays. This was made possible by dual-gain preamplifiers (Multi Channel Systems CPA16 [17]). The low-gain stage (0.09 V/pC) was set to shape pulses corresponding to energies
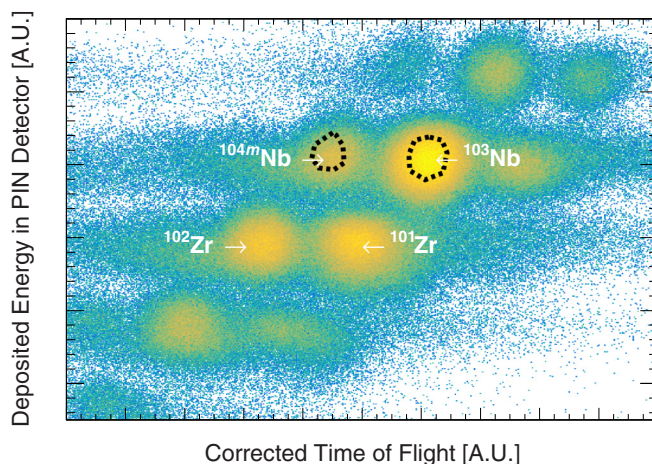

FIG. 1. The particle identification plot showing the two nuclei studied in the present work. Both deposited energy in the first silicon PIN detector and corrected ToF measurements are in arbitrary units. The four most intense beams in this experiment are labeled. The two-dimensional gates for ^{103}Nb and ^{104m}Nb are shown as dashed lines. Position measurements in the I2SCI were performed to correct the different momenta accepted through the A1900 fragment separator (see text for details).

of several GeV while the high-gain stage (1.63 V/pC) was set appropriately for energies of a few MeV. A threshold of 120 keV was applied on the high-gain DSSD signal during analysis to eliminate noise. A silicon surface barrier detector was located 25 mm behind the DSSD. This veto detector was used to eliminate light particles that passed through the DSSD. The average time between implantations in a single central pixel was approximately 12 seconds.

The DSSD was located at the center of the beam pipe and surrounded by the Summing NaI(Tl) detector (SuN). γ rays from the deexcitation of the excited daughter nuclei were measured in SuN. SuN is a right-circular cylindrical detector with eight segments of NaI(Tl) crystals. The energy deposited into each segment was determined by summing the energies read by three photomultiplier tubes. The large volume and high efficiency of SuN allows the total absorption spectroscopy (TAS) method to be employed. The histograms of each of the eight segment spectra were combined to produce the sum-of-segments spectrum. This sum-of-segments spectrum was sensitive to the energy of individual γ rays emitted from the excited daughter nuclei. The energies of each segment were summed on an event-by-event basis to produce the TAS spectrum. The TAS spectrum is sensitive to the energy levels of the daughter nucleus that were populated through β decay. The multiplicity plot was constructed by counting the number of segments in SuN that detected energy during the event. The multiplicity plot therefore depends on the number of γ rays emitted following a β decay. More information on the SuN detector can be found in Ref. [18].

The NSCL Digital Data Acquisition System (DDAS) was used for the measurements [19]. Signals from the DSSD were recorded if there were coincident signals from the front and back side of the DSSD. This was done to reduce background
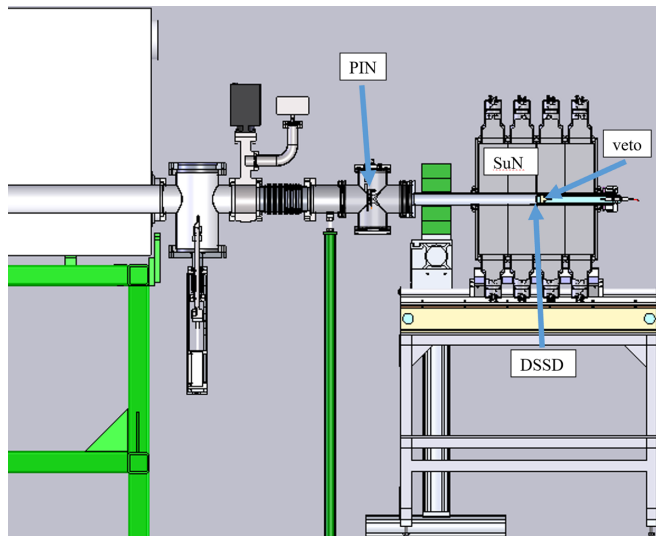
FIG. 2. Shown above is the detector layout of the e12001 experiment conducted at the NSCL.

noise. More details about the setup and electronics can be found in Refs. [15,16].

III. ANALYSIS

A. Correlations

There were two types of events of interest for this experiment: implantation events and decay events. The detector layout is shown in Fig. 2. An event was designated as an implantation event if there was a signal in both silicon PIN detectors, a signal in both sides of the low-gain DSSD, and no signal from the veto detector behind the DSSD. An event was designated as a decay event if there was no signal in either of the silicon PIN detectors, no signal in the low-gain DSSD, a signal from both sides of the high-gain DSSD, and no signal from the veto detector. Each decay event was then correlated with an implantation event if the implantation event occurred in the same pixel in the DSSD within a fixed time window before the decay event. This time window was chosen to be 20 s to evaluate the half-life and possible contamination. However, only correlation times less than one $T_{1/2}$ were included when compiling the experimental γ-ray spectra. Multiple decay events were allowed to be correlated to a single implantation event. The closest implantation in time was correlated to the decay event. If the candidate implantation event occurred within one second of another implantation event, the correlation was rejected. This correlation procedure will be called forward correlation (FC).

In addition to correctly correlating implantation and decay events, FC may correlate a β-decay event with an unrelated implantation event. To account for these random correlations, the correlation procedure was also performed backwards in time. Decay events were correlated to implantation events that happened in the same pixel in the DSSD, but happened after the decay event. This correlation violates causality and ensures that the implantation and decay event are not related.

TABLE I. Information about the analyzed nuclei. Half-lives for ^{103}Nb and ^{104m}Nb were taken from Ref. [16]. All other half-lives are from Ref. [21]. Half-lives for each nucleus are enclosed in parentheses.

Parent	^{103}Nb^{41+} (1.34 s)	^{104m}Nb^{41+} (0.97 s)
Daughter	^{103}Mo (67.5 s)	^{104}Mo (60.0 s)
Possible contaminants	^{101}Nb^{40+} (7.1 s)	^{102}Nb^{40+} (1.3 s)
	^{100}Nb^{40+} (1.5 s)	^{101}Nb^{40+} (7.1 s)

This correlation procedure will be called random correlation (RC).

The time difference between an implantation event and its correlated decay event is the decay time. Decay times for FC and RC are used in this technique to study the half lives of nuclei [16]. Often at long times it is observed that the RC decay events are more than the FC events. This is an unphysical behavior that appears due to the fixed number of implants correlated to β-decay events in forward and reverse time directions. For this reason, we used the number of events between 19 and 20 s to normalize the RC histogram. The adjustment was less than 15% in the two nuclei of interest and was also applied to the RC γ-ray spectra used in the present analysis.

The half-lives extracted from the experimental decay histograms further confirm correct particle identification. An extensive half-life analysis of ^{103}Nb (1.34 ± 0.07 s) and ^{104m}Nb (0.97 ± 0.1 s) was already published in Ref. [16]. Since the half-lives of ^{104}Nb and ^{104m}Nb were previously found to be 4.9 ± 0.3 s and 0.94 ± 0.04 s [20] respectively, it was concluded that this experiment predominantly populated ^{104m}Nb.

B. Experimental spectra

A summary of the basic properties of ^{103,104m}Nb is given in Table I. The experimental spectra, which consisted of TAS, sum-of-segments, and multiplicity spectra for each isotope, were constructed by selecting implantation events associated with each isotope and looking at the energy measurements in SuN from their correlated decay events. For each isotope studied here, only events with a correlation time of less than one $T_{1/2}$ were considered. This was done to reduce the ratio of random correlations to real correlations and to reduce the contribution of daughter decays. Charge state contaminants, ^{102}Nb^{40+} through ^{100}Nb^{40+}, were of concern for this experiment. To investigate possible contributions from charge state contaminants, the γ-ray and particle identification spectra were used. These possible contaminants have A/Q ratios similar to the isotopes of interest, but not identical. As such, they are expected to appear at different locations in the PID spectra overlapping, however, with the isotopes of interest. TAS and sum-of-segments spectra were used with different gating conditions that aimed at enhancing the expected contaminant contributions. However, no contaminant signatures were observed in the γ spectra. To additionally verify that there was minimal charge state contamination, PID gates were redrawn in areas where there would be a significantly greater

number of charge state contaminants. The resulting experimental spectra with these gates were compared to the spectra produced by the original PID gates. There were no significant changes. This investigation led to the conclusion that charge state contamination in the extracted experimental spectra was not significant (no greater than a few percent for both nuclei).

C. Simulation spectra

The $I_\beta(E)$ distribution was extracted from the experimental data using the forward folding procedure presented in Ref. [22]. To apply this technique, GEANT4 [23] was run to simulate the detection of β-decay electrons and β-delayed γ rays in each segment of SuN to account for detector resolution and efficiencies. Each simulation created a spectrum for TAS, sum of segments, and multiplicity in the same way it was done for the experiment. Thresholds in the DSSD and SuN segments were kept consistent with the experiment thresholds. Energy levels, spins, parities, and branching ratios were taken from the National Nuclear Data Center (NNDC) database [21] to generate cascades to simulate the population of each discrete energy level in the daughter nuclei ^{103,104}Mo.

Not all energy levels in ^{103,104}Mo up to the β-decay Q value of ^{103,104m}Nb were listed by the NNDC. There was a critical energy below which the level scheme was considered complete. The last known levels populated in β decay for ^{103}Mo and ^{104}Mo were 1.2 and 2.9 MeV, respectively, and these were taken to be the critical energies. DICEBOX [24], a statistical model code, was used to generate γ-ray cascades from so-called pseudoenergy levels above this critical energy for ^{103,104}Mo. Pseudoenergy levels represent the characteristics of closely spaced energy levels within the resolution of SuN. These pseudoenergy level simulations were done up to the highest energy level populated in the experiment for each nucleus as observed in the TAS spectra. For ^{103}Mo, the highest level populated was around 4.5 MeV. For ^{104}Mo, the highest level populated was around 7 MeV.

D. $I_\beta(E)$ extraction

The results from the simulation of each energy level in the daughter were used as components in a fitting program that varied the multiplicative coefficients to minimize χ^2. The multiplicative coefficient of all of the RC spectra were fixed in the fitting program. Nine experimental spectra were produced to feed into the reduced χ^2 fitting program. The TAS spectrum, the sum-of-segments spectrum, and the multiplicity spectrum are three of the spectra that were fitted. Six other spectra included in the same fit were produced by gating the sum-of-segments spectra and the multiplicity on TAS energy above 2.5 MeV, between 0.8 and 2.5 MeV, and below 0.8 MeV. These spectra were included in the fit to increase the sensitivity of the fitting procedure. The TAS spectrum, sum-of-segments spectrum, and multiplicity plots for ^{103}Nb and ^{104m}Nb are shown in Figs. 3 and 4, respectively, with least χ^2 fits. The multiplicative coefficients of each basis state determined by minimizing χ^2 corresponded to the un-normalized β intensities for each level. These coefficients were normalized to 100% to form the $I_\beta(E)$.
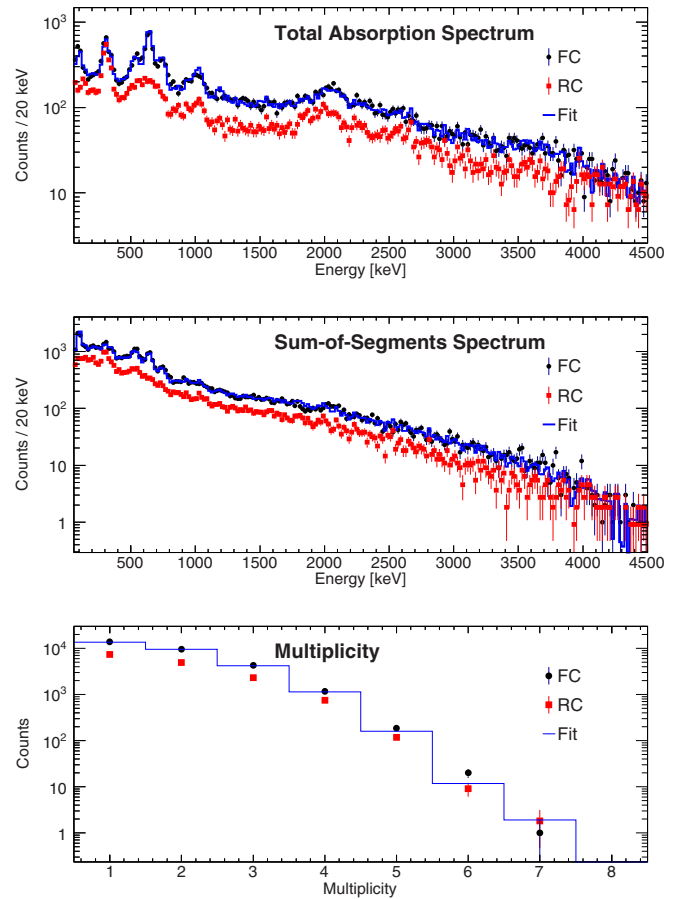

FIG. 3. The best fit to the data for the β decay of ^{103}Nb. Only three of the nine fitted spectra are shown. The best fits are the blue lines. The RC spectra are in red (square markers). The FC spectra are in black (circular markers). The RC spectra are well below the FC spectra which indicates that the FC spectra are not dominated by random correlations.

Not all daughter energy levels listed in the NNDC database have known spins. To investigate the impact of uncertain spin assignments to the experimentally determined $I_\beta(E)$, simulation and fitting were done for different spin assumptions. Randomizing the unknown spins changed the $I_\beta(E)$ for both ^{103,104m}Nb by less than 1%. This is insignificant compared to the standard deviation associated with the χ^2 fitting. The standard deviation associated with the χ^2 fitting was therefore taken to be the experimental uncertainty.

IV. RESULTS

The cumulative $I_\beta(E)$ and cumulative B(GT) for both ^{103,104m}Nb are presented in this section and compared to QRPA calculations. The B(GT) was calculated from the $I_\beta(E)$ with

$$B(\text{GT}) = \frac{I_\beta(E)}{f(Q_\beta - E)T_{1/2}} K \left(\frac{g_V}{g_A}\right)^2, \qquad (1)$$

where $f(Q_\beta - E)$ is the Fermi integral, K is 6143.6(17) s [25], g_A/g_V is $-1.270(3)$ [26], and the half-life was taken from Ref. [16].
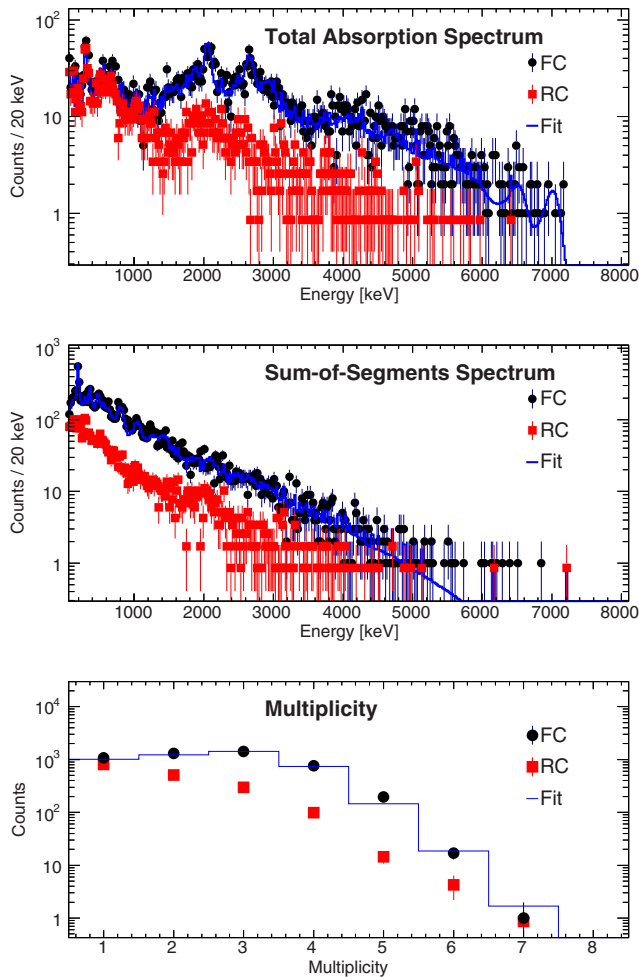
FIG. 4. The best fit to the data for the β decay of ^{104m}Nb. Only three of the nine fitted spectra are shown. The best fit are the blue lines. The RC spectra are in red (square markers). The FC spectra are in black (circular markers). The RC spectra are generally below the FC spectra which indicates that the FC spectra are not completely dominated by RC. FC is dominated by random correlations below 1 MeV.

FIG. 5. The cumulative $I_\beta(E)$ for ^{103}Nb is shown as a black line in (a). The cumulative B(GT) for ^{103}Nb is shown as a black line in (b). The shaded region indicates experimental uncertainty which corresponds to the minimum and maximum cumulative $I_\beta(E)$ and B(GT). The $5/2^+$ prolate calculation is shown as a dotted line. The $7/2^+$ oblate calculation is shown as a dashed line. The $5/2^+$ oblate calculation is shown as a dot-dashed line.

To obtain the QRPA result, we used an extension of the axially deformed Skyrme finite amplitude method (FAM) [27,28] that treats odd numbers of nucleons in the equal filling approximation (EFA) [29,30]. The method is fully self-consistent in this approximation. The Skyrme functional and single-particle space are the same as those used in the global calculation of Ref. [31], which fixed a single set of parameters to compute β-decay rates of almost 1400 neutron rich even-even isotopes. We used the parameters of fit 1A of Ref. [31] for the time-odd parts of the Skyrme functional, and adopted an effective axial-vector coupling constant g_A of 1.0. We applied a small artificial half-width of 0.005 MeV to strength functions to resolve all of the QRPA transitions without allowing the width to significantly contribute to the rate. As discussed in Ref. [28], the phase-space weighted combination of allowed and first-forbidden strength functions gives the shape factor, which when integrated over the allowed energy range gives 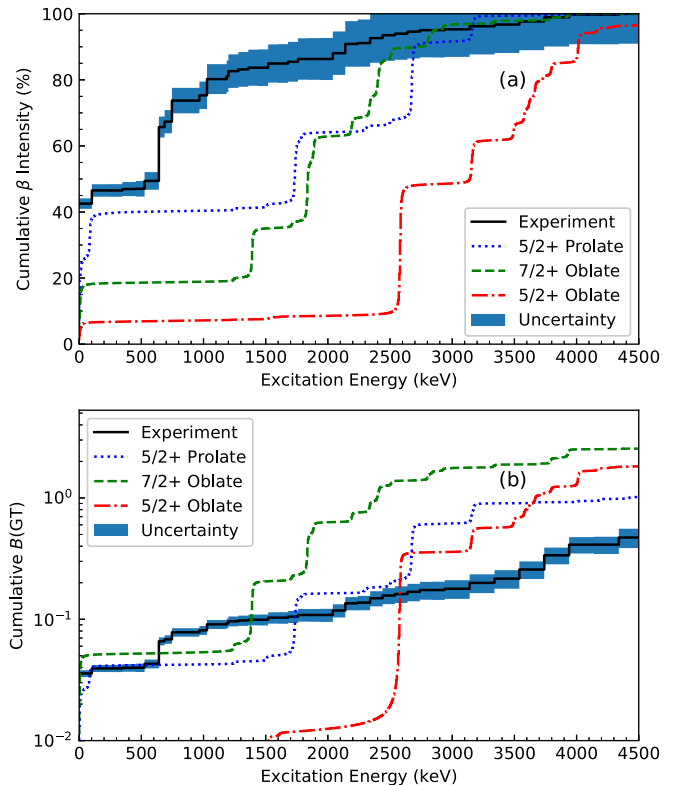the total rate. The feeding intensity is the cumulative integrated shape factor normalized to the total rate. To compare with experimental data, we took the lowest-energy QRPA state to be the daughter ground state and shifted all QRPA energies accordingly.

A. ^{103}Nb

Figure 5 shows the experimental cumulative $I_\beta(E)$ and B(GT) for ^{103}Nb along with QRPA calculations. The uncertainty bands represent the cumulative minimum and maximum $I_\beta(E)$ and B(GT). The fit was done in the range between 60 keV and 4.5 MeV in both the TAS spectrum and the sum-of-segments spectrum. Counts above 4.5 MeV were excluded from the fit because the data were dominated by random correlations. Pseudoenergy level simulations from DICEBOX were included to handle β decays to excited states between 1.2 and 4.5 MeV. The numerical values for the $I_\beta(E)$ for ^{103}Nb can be seen in Table II.

In our ^{103}Nb QRPA calculation, we considered multiple ground state configurations. The potential energy curve generated by constraining the quadrupole deformation of the neighboring even-even nucleus ^{104}Mo exhibits local minima at oblate and prolate deformations. We used the solutions at these two minima as reference vacua to carry out EFA

TABLE II. $I_\beta(E)$ for ^{103}Nb. All intensity values that were below 10^{-3}% were set to 0.

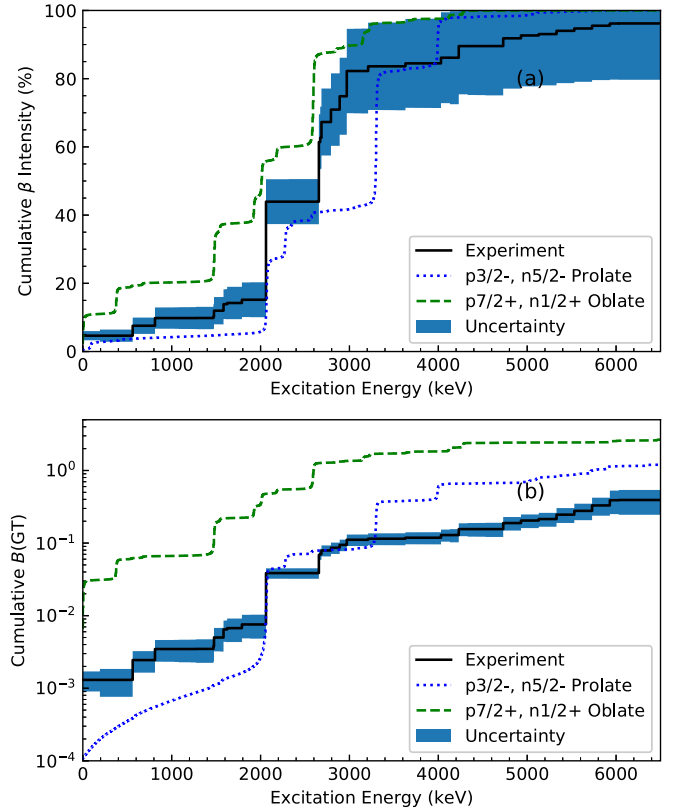| Energy (keV)	Intensity (%)	Error (±)	Energy (keV)	Intensity (%)	Error (±)
0	42.5	1.6	1680	0.53	0.18
102.6	4.0	0.3	1760	0.84	0.23
241.1	0		1840	0	
346.5	0.43	0.20	1940	0	
353.7	0		2040	1.76	0.21
433.2	0		2140	2.8	0.3
456.1	0.08	0.22	2240	0.26	0.24
489.8	0		2340	1.5	0.3
526.13	2.4	0.3	2440	0.89	0.26
641.1	16.3	0.5	2540	0.46	0.17
687.4	1.6	0.3	2640	0.60	0.21
692.8	0		2740	0.45	0.12
746.2	6.4	0.3	2840	0	
967.1	1.6	0.3	2940	0.36	0.08
1028.2	4.9	0.4	3140	0.91	0.17
1185.7	0.9	0.3	3340	0.53	0.08
1200	1.6	0.3	3540	0.93	0.10
1280	0.53	0.19	3740	1.26	0.15
1360	0.51	0.20	3940	0.80	0.10
1440	0		4140	0	
1520	1.27	0.24	4340	0.26	0.08
1600	0		4540	0.01	0.04

FIG. 6. The cumulative $I_\beta(E)$ for ^{104m}Nb is shown as a black line in (a). The cumulative B(GT) for ^{104m}Nb is shown as a black line in (b). The shaded region indicates experimental uncertainty which corresponds to the minimum and maximum cumulative $I_\beta(E)$ and B(GT). The $\pi 3/2^-$, $\nu 5/2^-$ prolate calculation is shown as a dotted line. The $\pi 7/2^+$, $\nu 1/2^+$ oblate calculation is shown as a dashed line.

calculations for all proton quasiparticle levels within about 1 MeV of the Fermi surface, taking the ground state to be the lowest-energy solution. That ground state turned out to be oblate, with a quadrupole deformation parameter of $\beta_2 = -0.199$, $T_{1/2} = 1.0$ s, and $J^\pi = 7/2^+$, in disagreement with the experimental result $J^\pi = 5/2^+$ in the ENSDF database [32]. The $5/2^+$ states appear in the our calculation at low excitation energy, with an oblate state at 0.493 MeV ($T_{1/2} = 1.1$ s) and a prolate state (a quadrupole deformation parameter of $\beta_2 = 0.343$ and $T_{1/2} = 3.1$ s) at 0.875 MeV. These results are in close agreement with those of the finite-range EFA calculations of Ref. [33], where it is suggested the discrepancy with experiment may be resolved by triaxial deformation. We computed the feeding intensities for the ground state as well as the two $5/2^+$ states. The best match to the experimental data is from the prolate $5/2^+$ state, but even with it we predict too much intensity at higher energies.

It is worth noting the high I_β to the ground state. The J^π of the ground state of ^{103}Nb is $\frac{5}{2}^+$ and the J^π for the ground state of ^{103}Mo is $\frac{3}{2}^+$. Therefore, the ground state to ground state transition is an allowed Gamow-Teller transition. This allowed transition to the ground state is prominent in the experimental data. Although no γ rays are emitted during this transition, the high-energy electrons can be detected in SuN.

The possibility of β-delayed neutron emission for ^{103}Nb was considered because the β-decay Q value for ^{103}Nb is above the neutron separation energy for ^{103}Mo by about 0.5 MeV. However, a study of neutron emission following β decay for nuclei in the neutron-rich Y to Tc isotope region

concluded that ^{103}Nb has a P_n of 0.05% ± 0.03% [34]. Therefore, neutron emission was not expected to affect the data in any significant way.

Figure 5 shows that the agreement between the QRPA calculations and our data is poor for ^{103}Nb. This fact is not entirely surprising: the Skyrme-QRPA is a tool for computing strength functions in *all* nuclei, and can fail to accurately reproduce portions of the strength in any individual nucleus, particularly one that has odd numbers of neutrons and/or protons (e.g., [15,35]). Even so, however, our QRPA calculations show a significant fragmentation of the β-decay strength as a function of energy, as do the data. The QRPA also reproduces the strength to the lowest state well.

B. ^{104m}Nb

The cumulative $I_\beta(E)$ and B(GT) for ^{104m}Nb are shown in Fig. 6. The numerical values for the $I_\beta(E)$ can be seen in Table III. This experiment populated the metastable state of ^{104}Nb which has a high but undetermined spin [36], as described in [16]. The value 4^+ was used in our analysis as guided by theory (see below). The strongest feeding goes to the 2061 keV level (28.8% ± 1.5%), with an additional strong feeding to the 2656 keV level (17.5% ± 1.5%). Neither of

TABLE III. $I_\beta(E)$ for ^{104m}Nb. All intensity values that were below 10^{-3}% were set to 0.

Energy (keV)	Intensity (%)	Error (±)	Energy (keV)	Intensity (%)	Error (±)
0	5.6	1.3	3050	0	
192	0		3130	0	
561	2.9	0.6	3210	1.4	0.4
812	2.2	0.7	3290	0	
886	0		3370	0	
1028	0		3450	0	
1080	0		3530	0	
1215	0		3630	0.87	0.14
1275	0.02	0.06	3730	0	
1469	0.4	0.3	3830	0	
1475	1.7	0.4	3930	0	
1545	0		4030	1.65	0.23
1583	1.9	0.3	4130	0.0	0.3
1607	0		4230	3.4	0.5
1611	0		4330	0.00	0.21
1624	0.3	0.3	4430	0	
1790	1.0	0.3	4530	0.00	0.08
1882	0		4730	2.3	0.3
2061	28.8	1.5	4930	0.84	0.21
2317	0		5130	0.40	0.11
2656	17.5	1.5	5330	1.0	0.3
2671	1.3	1.0	5530	0.7	0.3
2685	4.6	0.7	5730	0.8	0.3
2792	3.6	0.8	5930	0.6	0.5
2888	0		6030	0.02	0.07
2890	3.9	0.6	6530	1.6	0.3
2970	7.4	1.1	7030	2.2	0.5

these daughter levels has a confirmed spin assignment. The feeding to the ground state of ^{104}Mo is low (5.6% ± 1.3%) as expected due to the large spin difference. It should also be noted that the multiplicity spectrum for ^{104m}Nb peaks at much higher values compared to ^{103}Nb, which is another indication of the large spin difference between the spins of the populated levels and the ground state of ^{104}Mo.

In our ^{104}Nb QRPA calculations we used the same prolate and oblate ^{104}Mo reference vacua that we used for ^{103}Nb. We conducted EFA calculations for all combinations of one proton and one neutron states within about 1 MeV of their respective Fermi surfaces and found the ground state configuration to be $\pi\frac{7}{2}^+$, $\nu\frac{1}{2}^+$ with an oblate quadrupole deformation of $\beta_2 = -0.199$ and $T_{1/2} = 0.55$ s. The theoretical calculations in Ref. [37] suggest the ground state has a strong prolate deformation and a $\pi\frac{3}{2}^-$, $\nu\frac{5}{2}^-$ configuration. This prolate configuration appears in our calculation as a low lying state with excitation energy of 1.11 MeV and quadrupole deformation parameter of $\beta_2 = 0.378$ and $T_{1/2} = 3.3$ s. We calculated the feeding intensity for both the oblate ground state and the prolate configuration.

The uncertainty bands in Fig. 6 show the minimum and maximum cumulative $I_\beta(E)$ and B(GT). Figure 6 shows that QRPA gives better results than in ^{103}Nb. The prolate configuration seems to match experiment better. However, it tends to place more I_β at higher energies which, in return, places more B(GT) at higher energies. The Gallagher-Moszkowski rule [38] for computing spins of odd-odd nuclei yields $J^\pi = 4^+$ for both configurations considered in our QRPA calculations. However, the spin-parity assignments in Ref. [37] suggest this rule is broken in ^{104}Nb with the $\pi\frac{3}{2}^-$, $\nu\frac{5}{2}^-$ having $J^\pi = 1^+$. In any case, the prolate configuration would be consistent with ground state J^π between 1^+ and 4^+, which agrees with the above discussion for the ground state J^π.

V. CONCLUSIONS

The $I_\beta(E)$ distribution was measured for the first time for ^{103,104m}Nb in an attempt to test QRPA predictions for unstable nuclei relevant for the r process. The comparison with experimental data for ^{103,104m}Nb shows that QRPA exhibits strength fragmentation comparable to the experimental data and comparable half lives. The overall agreement, while improved compared to previous tests of QRPA calculations (e.g., in [35,39]), is not good over the entire energy range of the experiment, either for $I_\beta(E)$ or B(GT). As mentioned already, this is not terribly surprising given that Skyrme functionals are designed to reproduce global properties and the Skyrme-QRPA is a relatively simple approximation. We are currently working to improve the method by incorporating beyond-QRPA correlations. In the future, these improved QRPA calculations can be used to increase the reliability of r-process models.

Future plans include experimental studies of nuclei in the same mass region as well as studies of nuclei in other accessible mass regions, in order to provide more data for a systematic comparison to theoretical calculations.

[1] K. M. Burbidge, G. R. Burbidge, W. A. Fowler, and F. Hoyle, Rev. Mod. Phys. **29**, 547 (1957).

[2] A. G. W. Carmeron, Publ. Astron. Soc. Pac. **69**, 201 (1957).

[3] M. Arnould and S. Goriely, Phys. Rep. **384**, 1 (2003).

[4] T. Rauscher, N. Dauphas, I. Dillmann, C. Frohlich, Z. Fulop, and G. Gyurky, Rep. Prog. Phys. **76**, 066201 (2013).

[5] B. P. Abbott *et al.*, Phys. Rev. Lett. **119**, 161101 (2017).

[6] D. Kasen, B. Metzger, J. Barnes, E. Quataert, and E. Ramirez-Ruiz, Nature (London) **551**, 80 (2017).

[7] D. Watson *et al.*, Nature (London) **574**, 497 (2019).

[8] B. Pfeiffer, K. L. Dratz, F. K. Thielemann, and W. B. Walters, Nucl. Phys. A **693**, 282 (2001).

[9] M. R. Mumpower, R. Surman, G. C. McLaughlin, A. Aprahamian., Prog. Part. Nucl. Phys. **86**, 86 (2016).

[10] P. Möller, J. R. Nix, and K.-L. Kratz, At. Data Nucl. Data Tables **66**, 131 (1997).

[11] P. Möller, J. R. Nix, W. D. Myers, and W. J Swiatecki, At. Data Nucl. Data Tables **59**, 185 (1995).

[12] C. L. Duke, P. G. Hansen, O. B. Nielsen, and G. Rudstam, Nucl. Phys. A **151**, 609 (1970).

[13] P. Dimitriou and A. L. Nicholas, *Total Absorption Gamma-ray Spectroscopy for Decay Heat Calculations and Other Applications* (IAEA, Vienna, 2015).

[14] D. J. Morrissey, B. M. Sherril, M. Steiner, A. Stolz, and I. Wiedenhoever, in 14th International Conference on Electromagnetic Isotope Separators and Techniques Related to their Applications [Nucl. Instrum. Methods Phys. Res., Sect. B **204**, 90 (2003)].

[15] A. C. Dombos, Ph.D. thesis, Michigan State University, 2018; A. C. Dombos *et al.*, Phys. Rev. C **103**, 025810 (2021).

[16] A. C. Dombos *et al.*, Phys. Rev. C **99**, 015802 (2019).

[17] Multi Channel Systems, Markwiesenstrasse 55, D-72770 Reutlingen, Germany, phone 49 (0) 71 21 / 50 30 10, www.multichannelsystems.com.

[18] A. Simon *et al.*, Nucl. Instrum. Methods Phys. Res., Sect. A **703**, 16 (2013).

[19] C. J. Prokop, S. N. Liddick, B. L. Abromeit, A. T. Chemeny, N. R. Larson, S. Suchyta, and J. R. Tompkins, Nucl. Instrum. Methods Phys. Res., Sect. A **741**, 163 (2014).

[20] M. J. Martin, Nucl. Data Sheets **114**, 1497 (2013).

[21] National Nuclear Data Center, www.nndc.bnl.gov/nudat2.

[22] A. C. Dombos, D.-L. Fang, A. Spyrou, S. J. Quinn, A. Simon, B. A. Brown, K. Cooper, A. E. Gehring, S. N. Liddick, D. J. Morrissey, F. Naqvi, C. S. Sumithrarachchi, and R. G. T. Zegers, Phys. Rev. C **93**, 064317 (2016).

[23] S. Agostinelli *et al.*, Nucl. Instrum. Methods Phys. Res., Sect. A **506**, 250 (2003).

[24] F. Bečvář, Nucl. Instrum. Methods Phys. Res., Sect. A **417**, 434 (1998).

[25] J. C. Hardy and I. S. Towner, Nucl. Phys. News **16**, 11 (2006).

[26] J. C. Hardy and I. S. Towner, Phys. Rev. C **79**, 055502 (2009).

[27] P. Avogadro and T. Nakatsukasa, Phys. Rev. C **84**, 014314 (2011).

[28] M. T. Mustonen, T. Shafer, Z. Zenginerler, and J. Engel, Phys. Rev. C **90**, 024308 (2014).

[29] T. Shafer, J. Engel, and C. Fröhlich, G. C. McLaughlin, M. Mumpower, and R. Surman, Phys. Rev. C **94**, 055802 (2016).

[30] S. Perez-Martin and L. M. Robledo, Phys. Rev. C **78**, 014304 (2008).

[31] M. T. Mustonen and J. Engel, Phys. Rev. C **93**, 014304 (2016).

[32] Evaluated Nuclear Structure Data Files (ENSDF), http://www.nndc.bnl.gov/ensdf.

[33] R. Rodriguez-Guzman, P. Sarriguren, and L. M. Robledo, Phys. Rev. C **83**, 044307 (2011).

[34] T. Mehren, B. Pfeiffer, S. Schoedder, and K.-L. Dratz, Phys. Lett. **77**, 458 (1996).

[35] S. Lyons *et al.*, Phys. Rev. C **100**, 025806 (2019).

[36] M. Graefenstedt, U. Keyser, F. Münnich, F. Schreiber, H. R. Faust, and H. Weikard, Z. Phys. A: At. Nucl. **327**, 383 (1987).

[37] Y. X. Luo *et al.*, Phys. Rev. C **89**, 044326 (2014).

[38] C. J. Gallagher and S. A. Moszkowski, Phys. Rev. **111**, 1282 (1958).

[39] A. Spyrou *et al.*, Phys. Rev. Lett. **117**, 142701 (2016).